Finite-temperature investigation of homovalent and heterovalent substituted $BaTiO_3$ from first principles

Florian Mayer[1,*] Maxim N. Popov[1] Petr Ondrejkovic[2] Jiri Hlinka[2] Jürgen Spitaler[1] and Marco Deluca[1]
[1]*Materials Center Leoben Forschung GmbH, Roseggerstrasse 12, 8700 Leoben, Austria*
[2]*Institute of Physics of the Czech Academy of Sciences, 182 00, Praha 8, Czech Republic*

(Received 2 November 2022; accepted 8 December 2022; published 23 December 2022)

Barium titanate (BT) solid solutions are used in a wide range of applications such as piezoelectric actuators and high-performance energy storage devices. The key to achieve and tune desired macroscopic properties is the chemical modification, which is done by substituting Ba or Ti with other homovalent or heterovalent cations. This work uses large-scale molecular dynamics simulations based on an effective Hamiltonian approach to calculate the macroscopic properties of BT solid solutions from first principles, thereby offering a framework for the prediction of properties prior to materials synthesis. To this end, we elaborate on the theoretical description of substitution in effective Hamiltonians as well as their parametrization by density functional theory calculations for two model systems: homovalent substituted $BaZr_xTi_{1-x}O_3$ (BZT) and heterovalent substituted $BaNb_xTi_{1-x}O_3$ (BNT). The effective Hamiltonian for BZT obtained in this work is first used for benchmarking against other models and experimental data on the phase diagrams and dielectric properties. Subsequently, the effective Hamiltonian is further extended and used to parametrize BNT and compare the model's predictions to the available experimental data. The parameter sets obtained in this work can be used for future studies and provide deep insight into the subject of relaxor ferroelectrics.

DOI: 10.1103/PhysRevB.106.224109

I. INTRODUCTION

Relaxor ferroelectrics (RFs) have recently been the subject of intensive investigations as possible energy storage materials with both high power and energy density [1–3]. RFs, in essence, are ferroelectrics where the long-range polarization correlation is disrupted [1] due to chemical substitution. On the macroscopic scale, this results in a reduction of the hysteretic losses originating from the reorientation of polar domains, which increases the recoverable energy density. Other parameters play a role in achieving high energy density, for instance, a high saturated polarization, small leakage currents, and a high breakdown voltage. As permittivity (and thus saturation polarization) decreases with the loss of ferroelectric character, one issue is how to stabilize a high permittivity in a RF. These aspects are intimately related with how the chemical substitution affects the local lattice structure, its polar order, and how the material interacts with external applied electric fields at atomic scale and on the mesoscale. It is thus very important to be able to predict macroscopic electrical properties in such systems at finite temperatures and external fields, starting from simulated atomic scale structures. In other words, realistic molecular dynamics (MD) simulations need to be performed to investigate substitution effects at the atomic level and their impact on the material's properties.

In this work, we provide an improved model of the potential energy surface for the application in MD simulations. Our approach is based on so-called effective Hamiltonians [4,5], first introduced in the early 1990s for perovskites. The required parameters for the effective Hamiltonians can entirely be determined by first-principles calculations. Furthermore, a significant advantage of this approach is the computational efficiency due to the reduced number of degrees of freedom. In the beginning, this model was a mean-field theory [5], which was later adapted to a local-mode framework [6]. In 2010, Nishimatsu *et al.* [7] revised this model, improving its accuracy. Paul *et al.* [8] showed that including anharmonic couplings further enhances the quality of such simulations. In our previous work [9], we established a more general approach for including these couplings, which improved the description of both phase transitions and dielectric properties. Here we build upon our previous findings and use the parameter set for pure barium titanate (BT) as the basis for the parametrization of effective Hamiltonians for substituted systems. In literature, such effective Hamiltonians for substituted systems are found with different approaches for incorporating the substituted ions. This includes the parametrization by the virtual crystal approximation [10,11], by adding additional terms to the Hamiltonian [12–14], or simply treating the system by averaging [15] parameters of two constitutive systems. The present work introduces an alternative approach based on the following principles. First, the used Hamiltonian of the parent system BT builds on a revised parametrization [9] including a large number of anharmonic couplings to higher energy phonons. That increases the accuracy of the potential energy surface as well as the quantitative description of the transition temperatures [9]. Second, the substituted ions are incorporated as perturbation to the pure BT system using a revised treatment of interactions. Thus, special consideration

*florian.mayer@mcl.at

is given to the local description of the occurring substitution effects. In addition, the presented effective Hamiltonian is independent of concentration and hence the parametrization procedure is more flexible and has to be performed only once.

To test our approach, we parametrize two fundamentally different RF systems: one homovalent and one heterovalent substituted BT. In the former case, Ti^{4+} ions on the B-site are substituted by Zr^{4+} ions, leading to the $BaZr_xTi_{1-x}O_3$ (BZT) solid solution. For the heterovalent case, Ti^{4+} are substituted by Nb^{5+}, which yields $BaNb_x\square_{1/4x}Ti_{1-5/4x}O_3$ (BNT). Here, it is essential to consider the presence of Ti vacancies for charge compensation as discussed in detail in a former publication [16]. The BZT Hamiltonian serves as the basis for a benchmark to test our model and its assumptions. For BZT, the effective Hamiltonians are already available, however, they lack the incorporation of additional anharmonic couplings. These references offer the possibility to test our approach. Furthermore, a cross check between simulations and experimental data is presented. In the case of BNT, we are not aware of any existing parametrizations, and therefore we rely on experimental data to carry out a comparison with the simulations.

The cornerstone of this investigation is the alternative parametrization of our models from density functional theory (DFT) calculations. DFT was already used in one of our previous publications [16] to study the effects of the above-mentioned substituents in a static picture in terms of local volume change and impact on electrical potential. The present paper continues our previous work by expanding the effective Hamiltonian towards substituted systems, as presented in Sec. II. Subsequently, we discuss the parametrization of BZT by DFT calculations, followed by a benchmark of this Hamiltonian with other models and experimental data. Building on this, the parametrization of BNT is presented, followed by application of the model for simulating the phase diagram and dielectric properties, and the comparison with the experiments.

II. THEORETICAL FRAMEWORK

A. Effective Hamiltonian of pure BT

The basis of our simulations is the effective Hamiltonian defined by Nishimatsu *et al.* [7,17], as stated in Eq. (1). This Hamiltonian is used to describe the pure BT system. The required parameters can be obtained by DFT calculations and are discussed in the next section. In general, this Hamiltonian consists of the following energy contributions: Kinetic energies of the optical soft-mode $\boldsymbol{u}$ and the acoustic mode $\boldsymbol{w}$, local-mode self-energy V^{self}, dipole-dipole interaction V^{dpl}, short-range interaction V^{short}, elastic energies V^{elas}, strain-phonon interactions V^{coupl}, and interaction with an external field. The time derivatives of the variables are represented by $\dot{u}_\alpha$ and $\dot{w}_\alpha$, where α denotes the Cartesian component. $\boldsymbol{R}$ represents a translation vector indicating the position of the unit cells within the supercell. η_i are strain variables in Voigt notation. Z^* is the Born effective charge associated with the soft mode $\boldsymbol{u}$. The brackets $\{\}$ indicate a set of amplitudes u within a supercell. M^*_{dipole} and M^*_{acoustic} are the effective masses of the soft mode and the acoustic mode in the long wavelength limit, respectively. The parameter ϵ allows applying an external field. It should be mentioned here that for the soft mode a local basis by lattice Wannier functions (LWFs) [18,19] centered on the B cation was chosen. This also applies to all further calculations in which the soft mode and its displacement pattern are used.

$$\begin{aligned} H^{\text{eff}}_{\text{BTO}} = {} & \frac{M^*_{\text{dipole}}}{2}\sum_{R,\alpha}\dot{u}^2_\alpha(\boldsymbol{R}) + \frac{M^*_{\text{acoustic}}}{2}\sum_{R,\alpha}\dot{w}^2_\alpha(\boldsymbol{R}) \\ & + V^{\text{self}}(\{\boldsymbol{u}\}) + V^{\text{dpl}}(\{\boldsymbol{u}\}) + V^{\text{short}}(\{\boldsymbol{u}\}) \\ & + V^{\text{elas,homo}}(\eta_1,\ldots,\eta_6) + V^{\text{elas,inho}}(\{\boldsymbol{w}\}) \\ & + V^{\text{coupl,homo}}(\{\boldsymbol{u}\},\eta_1,\ldots,\eta_6) + V^{\text{coupl,inho}}(\{\boldsymbol{u}\},\{\boldsymbol{w}\}) \\ & - Z^*\sum_R \epsilon\ \cdot u(\boldsymbol{R}). \end{aligned} \tag{1}$$

B. Substitution via perturbation of BT

To extend the formalism for substituted systems, we add an additional term to the effective Hamiltonian of Eq. (1). This term accounts for effects induced by the presence of substituents. Compared to some previous work in this area, we are not using an averaged system as basis and, therefore, treat the substituents in terms of a perturbation to the Hamiltonian of the pure system [14]. A general form of the extended Hamiltonian is stated in Eqs. (2) and (3). The new symbolic variable σ is used to differentiate between unit cells with different B-site ions (e.g. $\sigma = \text{Ti, Zr, Nb, V}_{\text{Ti}}$).

$$\begin{aligned} & H^{\text{eff}}_{\text{total}}(\{\boldsymbol{u}\},\{\boldsymbol{w}\},\eta_i,\{\sigma\}) \\ & \quad = H^{\text{eff}}_{\text{BTO}}(\{\boldsymbol{u}\},\{\boldsymbol{w}\},\eta_i) + H^{\text{perturb.}}(\{\boldsymbol{u}\},\{\boldsymbol{w}\},\{\sigma\}), \end{aligned} \tag{2}$$

$$\begin{aligned} H^{\text{perturb.}} = {} & \Delta T(\{\boldsymbol{u}\},\{\boldsymbol{w}\},\{\sigma\}) + \Delta V^{\text{self}}(\{\boldsymbol{u}\},\{\sigma\}) \\ & + \Delta V^{\text{dpl}}(\{\boldsymbol{u}\},\{\sigma\}) + V^{\text{aux}}(\{\boldsymbol{u}\},\{\boldsymbol{w}\},\{\sigma\}). \end{aligned} \tag{3}$$

The perturbation term is inspired by former works of Bellaiche *et al.* [10,12,13] as well as Mentzer *et al.* [14] and consists of four different adaptations to the total energy as written in Eq. (3). The first term ΔT accounts for different effective masses and, therefore, the influence on the kinetic energies of the optical soft-mode and the acoustic branch.

The second term ΔV^{self} adapts the local-mode self-energy by introducing the new parameters $\Delta\kappa_{2,\sigma}$, $\Delta\alpha_\sigma$, $\Delta\gamma_\sigma$ and $\Delta k_{1,\sigma}$ to $\Delta k_{4,\sigma}$. These parameters account for the change in local-mode self-energy when the B site is substituted with different ions compared to Ti. The complete form of this energy contribution is written below:

$$\begin{aligned} & \Delta V^{\text{self}}(\{\boldsymbol{u}\},\{\sigma\}) \\ & \quad = \sum_R \Big\{ \Delta\kappa_{2,\sigma}u^2(\boldsymbol{R}) + \Delta\alpha_\sigma u^4(\boldsymbol{R}) \\ & \qquad + \Delta\gamma_\sigma\left[u^2_y(\boldsymbol{R})u^2_z(\boldsymbol{R}) + u^2_z(\boldsymbol{R})u^2_x(\boldsymbol{R}) + u^2_x(\boldsymbol{R})u^2_y(\boldsymbol{R})\right] \\ & \qquad + \Delta k_{1,\sigma}u^6(\boldsymbol{R}) + \Delta k_{2,\sigma}\left(u^4_x(\boldsymbol{R}) * \left[u^2_y(\boldsymbol{R}) + u^2_z(\boldsymbol{R})\right]\right. \\ & \qquad \left. + u^4_y(\boldsymbol{R}) * \left[u^2_z(\boldsymbol{R}) + u^2_x(\boldsymbol{R})\right] + u^4_z(\boldsymbol{R}) * \left[u^2_x(\boldsymbol{R}) + u^2_y(\boldsymbol{R})\right]\right) \\ & \qquad + \Delta k_{3,\sigma}u^2_x(\boldsymbol{R})u^2_y(\boldsymbol{R})u^2_z(\boldsymbol{R}) + \Delta k_{4,\sigma}u^8(\boldsymbol{R})\Big\}. \end{aligned} \tag{4}$$

A further correction is made for the long-range interaction ΔV^{dpl} between dipoles. Since different B-site ions exhibit different Born effective charges, the Z^* must be adjusted accordingly. As a further correction, we introduce a term according to Refs. [10,12]. For the remainder of this paper, we call this term an auxiliary spring system. That is applied to compensate for the interaction of neighboring unit cells with different B-site ions:

$$V^{\mathrm{aux}}(\{\boldsymbol{u}\},\{\boldsymbol{w}\},\sigma) = \sum_{R}\sum_{T} Q_{T,R}(\sigma_T)\boldsymbol{e}_{T,R}\cdot\boldsymbol{u}(\boldsymbol{R}) + \sum_{R}\sum_{T} S_{T,R}(\sigma_T)\boldsymbol{f}_{T,R}\cdot\boldsymbol{w}(\boldsymbol{R}). \quad (5)$$

In detail, the term in Eq. (5) is used to calculate the influences of adjacent unit cells on the dynamics of the local mode $\boldsymbol{u}(\boldsymbol{R})$ and the acoustic displacement variables $\boldsymbol{w}(\boldsymbol{R})$. Here, the parameters $Q_{T,R}(\sigma_T)$ and $S_{T,R}(\sigma_T)$ account for differences between the substituted system's interactions compared to the pure system's interactions. $\boldsymbol{T}$ denotes the translation to unit cells up to the third nearest neighbor shell (3NN). $\boldsymbol{e}_{T,R}$ represents a unit vector joining the site $\boldsymbol{T}$ to the center of $\boldsymbol{u}(\boldsymbol{R})$. Analogously, the unit vector $\boldsymbol{f}_{T,R}$ is joining the site $\boldsymbol{T}$ with the center of $\boldsymbol{w}(\boldsymbol{R})$. At present, we restrict the auxiliary spring system to the first order [10] in $\boldsymbol{u}(\boldsymbol{R})$ and $\boldsymbol{w}(\boldsymbol{R})$, but it can be systematically expanded to higher orders, if required. As a final correction, we want to include the effects of lattice expansion or contraction in terms of homogenous strain induced by impurity ions. To compensate for these volume changes in the extended Hamiltonian, we apply a hydrostatic pressure [14,15] as a function of concentration. It should be noted, that this volume change directly affects the correction parameters $S_{T,R}(\sigma_T)$. In principle, these parameters would have to be determined individually for each concentration, but we decided to keep them constant in order not to lose the flexibility of the approach. This assumption is a good choice for small concentrations, but for higher concentrations an overestimation of local distortions can occur.

The parameterization of the extended Hamiltonian by first-principles calculations is detailed in the next section. For using the adapted Hamiltonian for MD simulations, we customized the *feram* code developed by Nishimatsu *et al.* [7,17,20].

C. Computational details

For all first-principles calculations, we used the projector-augmented [21] DFT package VASP [22–25] and the PBEsol [26] as exchange-correlation functional. An energy cutoff of 520 eV was used throughout all calculations. More details on DFT calculations and the following parametrization can be found in the Supplemental Material [27]. To increase the accuracy of the potential energy surface of pure BT, a large number of anharmonic couplings to higher energy phonons were considered, as described in detail in our previous publication [9]. These couplings were determined by an elaborate fitting procedure, as described in Ref. [9].

1. Parametrization of BZT

The parametrization of the extended Hamiltonian for BZT by means of DFT calculations is discussed here. First, we calculated the parameters for the adapted local-mode self-energy using a 5-atom unit cell. The lattice constant of this unit cell was set to that of pure BT ($a_i = 3.987$ Å) [9]. Subsequently, the B-site was replaced by Zr. The unit cell served as the basis for the calculation of displaced structures given by the displacement pattern of the soft-mode found in cubic BT (see Ref. [9] for the pattern). These displacements were constructed for directions ⟨001⟩, ⟨011⟩, and ⟨111⟩, respectively, whereby DFT was used to calculate the total energy. For the 5-atom unit cell calculations, a k grid size of $8 \times 8 \times 8$ was chosen. The results were then used to fit the Eqs. (14a)–(14c) from Ref. [7]. The resulting parameters are listed in the Supplemental Material [27] in Table SI. The calculation of the parameter $\Delta\kappa_2$ was performed as follows. $2 \times 2 \times 2$ supercells were constructed from the 5-atom unit cells. These were used to perform linear-response calculations (DFPT). The k grid was set to $4 \times 4 \times 4$. The phonon band structure was calculated for the respective systems from these calculations. Subsequently, the procedure as in Ref. [7] was used to determine short-range parameters. From this, the parameters $\Delta\kappa_2$ for BZT were determined (see Table SI in the Supplemental Material [27]). The DFPT calculations just mentioned were also used to calculate Z^* for a Zr unit cell, obtained from the Born effective charges.

For the calculation of the parameters for the auxiliary spring system, as a first step, a $3 \times 3 \times 3$ supercell of pure BT was constructed. Subsequently, one B site in this supercell was substituted with Zr. The atoms of the local unit cell containing the substituted atom were then displaced in discrete steps using the displacement pattern of the soft mode of pure BT. DFT was then used to calculate the total energy of the system and the forces acting on the atoms. Here, a k grid of size $2 \times 2 \times 2$ was chosen. From these data, the parameters $Q_{T,R}(\sigma_T)$ were determined using the total energies and fitting a linear function. To avoid double-counting, contributions were already taken into account by the Hamiltonian of pure BT, a reference system was calculated, and the corresponding total energies were subtracted from the substituted supercells. That procedure was repeated by displacing local unit cells up to the 3NN shells with respect to the substituted Zr ion. For the interaction between two Zr unit cells, two Zr ions were substituted as nearest neighbors. The calculation of the parameters is analogous to the above-mentioned procedure. The correction parameters $S_{T,R}(\sigma_T)$ were calculated using a A-centered basis and displacing the ions according to a translational eigenvector. Here, also the lattice constant was adapted to get the correction parameters in accordance with the lattice change already captured by the applied pressure correction. The estimation of the parameters using the total energy is analogous to the procedure described for $Q_{T,R}(\sigma_T)$. All results of the parameters discussed here are listed in Table SII in the Supplemental Material [27].

Next, a pressure correction was calculated to describe the Zr induced expansion or contraction of the lattice. For this purpose, the dependence of the BT lattice constant on an external pressure was first calculated using DFT. Then, a supercell of size $2 \times 2 \times 2$ was constructed and substituted with different concentrations of Zr. The full range of concentrations was used. These structures were relaxed using DFT and thus a dependence of a pseudocubic lattice parameter on

concentration was calculated. Using both results, a linear pressure correction of the magnitude $P(x) = -19.5x$ GPa could be calculated, where x denotes the concentration of Zr. From this result, it is clear that Zr exerts a negative pressure on the lattice, causing it to expand. This pressure correction is in good agreement with results of Mentzer *et al.* [14]; the small deviations can be explained by the different choice of the exchange-correlation functional. The corresponding plots of the pressure and concentration dependence of the lattice parameter can be found in the Supplemental Material [27], Figs. S1–S3.

2. Parametrization of BNT

As a next step, we parameterized an effective Hamiltonian for BNT. The main difference to BZT stems here from the heterovalency of Nb. This leads to charge compensation by Ti vacancies (V_{Ti}), as discussed in Ref. [16]. Thus, we simultaneously introduced Nb and V_{Ti} into the effective Hamiltonian, rather than Nb alone. To probe the effect caused by the introduction of these species, DFT calculations were performed on $5 \times 5 \times 5$ supercells; the results of which are shown in our previous work [16]. It turns out that the titanium vacancy has a considerable influence [16] on the surrounding unit cells. The unit cell containing V_{Ti}, on the other hand, contributes with its local dipole moment only to a limited extend to the polar order of the system. This is based on the observation from phonon calculations where the unit cells with Ti vacancies couple to the relevant polar modes of the surrounding unit cells only by a nonpolar oxygen oscillation. Owing to that, these unit cells are henceforth considered static with a zero net dipole. Consequently, the effective Hamiltonian was extended by another species σ and its associated parameters. The interactions of Ti vacancies with surrounding unit cells were considered by the parameters $Q_{T,R}(\sigma_T)$. The parameters for the adapted self-energy are not needed for the Ti vacancy since these unit cells are fixed with respect to the variable u for the simulation. What remains are the parameters of the auxiliary spring system for the interactions between the unit cells Ti-Nb, Ti-V_{Ti}, Nb-V_{Ti}, and Nb-Nb, as well as the adapted self-energy, effective mass, and Born effective charge for Nb unit cells. The parameterization of the latter is analogous to that for the case of BZT, but a suitable charge compensation has to be applied in the DFT calculations. The calculation of the parameters $Q_{T,R}(\sigma_T)$ was thus carried out as follows: A $3 \times 3 \times 3$ supercell was first prepared from pure cubic BT, then, for the calculation of Ti-Nb interactions, one B site was substituted with Nb. For Nb-Nb interaction, two Nb ions were introduced. The interaction between Ti or Nb unit cells with Ti vacancies was calculated by removing one Ti ion from the first coordination shell within the supercell. Subsequently, all supercells were calculated with DFT, and the resulting total energies were used to determine the parameters. The rest of the procedure is analogous to BZT. The estimation of the correction parameters $S_{T,R}(\sigma_T)$ for the acoustic displacement variables was carried out analogously to the procedure explained for BZT. All parameters derived for BNT are listed in the Supplemental Material [27]. The pressure correction must be computed also for BNT to account for any changes in the lattice due to substitution, and we can use the pressure dependence of the BT lattice parameter, analogous to BZT. The following calculations were then performed to estimate the dependence of the lattice parameter on the Nb concentration. Supercells of size $2 \times 2 \times 2$ and $3 \times 3 \times 3$ were used to substitute one or more sets of four Nb ions and one Ti vacancy. Subsequently, these structures were relaxed using DFT and a pseudocubic lattice constant was calculated. This results in a pressure correction of magnitude $P(x) = -8x$ GPa, where x is the concentration of Nb ions. This outcome reveals that Nb also induces an expansion of the lattice, which is, however, smaller as compared to BZT.

3. MD simulations

For the supercells used for MD simulations, the question of the distribution of substituted atoms arises. In the case of BZT, a random distribution [28] as well as a slight clustering [29–31] of Zr ions have been reported experimentally. In our case, we also tested different distributions, but finally convened on a randomly distributed arrangement of Zr ions. First of all, we determined effective cluster interactions from VASP supercell calculations, which were then used to perform Monte Carlo (MC) simulations to determine chemical ordering as a function of temperature [32]. The MC simulations showed that for experimentally relevant temperatures no ordering is found. In order to generate the disordered supercells, a random generator was used to create input structures for MD simulations. A simulation box of size $30 \times 30 \times 30$ was chosen. Subsequently, a series of structures with different concentrations of Zr were prepared. An MD run with the following settings was performed for each of these structures. A velocity-scaling algorithm was used to cool the system from 800 K to 20 K in steps of 5 K. At each temperature, the system was thermalized for 200 ps and averaged over 600 ps with a discrete-time step of 2 fs. The output configuration of dipoles was used as the initial condition for the following temperature. All simulations were carried out in the canonical ensemble. The obtained results made it possible to derive the phase diagrams. The transition temperatures were determined using the following procedures. For concentrations below the tricritical point, the results of polarization vs temperature and the change in shape of the simulation cell as a function of temperature were used. For concentrations beyond the tricritical point, the permittivity as a function of temperature was used to estimate T_m. The random distribution as determined by the MC simulation yields the best agreement of the phase diagram with experiments.

III. RESULTS

A. Simulations for BZT

1. Phase diagram

As the first step, we use our obtained model to simulate the phase diagram of BZT as a function of temperature and concentration. The simulation results of the phase diagram for BZT are presented in Fig. 1(a). It can be seen that the transition temperature between the paraelectric and ferroelectric phase initially decreases almost linearly with Zr concentration. At about 35% Zr content, this transition begins to flatten out. The transition boundaries between the

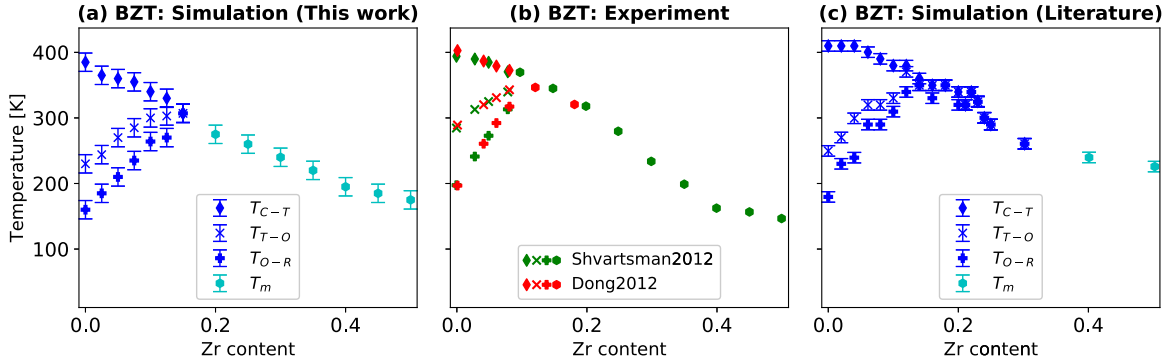

FIG. 1. Phase diagram of BZT simulated with effective Hamiltonians (a),(c) and experimentally observed values (b). The experimental values are from Refs. [1,33]. The simulated data from literature were taken from Ref. [14]. T_{C-T}, T_{T-O}, T_{O-R} transitions between cubic (C), tetragonal (T), orthorhombic (O), and rhombohedral (R) phases, respectively. T_m temperature of maximum in dielectric permittivity.

tetragonal and orthorhombic phase, and between the rhombohedral and orthorhombic phase increase significantly with Zr content until they merge at the tricritical point, which is located at about 12.5% Zr content. Compared to the experiment [1,33] [see Fig. 1(b)], our simulations yield slightly lower transition temperatures for concentrations between 0 and 30% of Zr. For higher concentrations, the simulated transition temperatures slightly overestimate the experimental data. This indicates that the pressure correction for this region of concentrations might be too strong. Furthermore, it should be noted that the transition temperatures depend relatively strongly on the distribution of Zr ions. Overall, the shape of the phase diagram is reproduced very well. Figure 1(c) shows simulation results from the literature [14], which were calculated using a different effective Hamiltonian. The difference lies on the one hand in the procedure of parameterization of the Hamiltonian for pure BT and on the other hand in the inclusion of substituted unit cells. For the latter, the application of a concentration-dependent pressure and the use of a restoring force was chosen in the work of Mentzer *et al.* [14]. The first term is equivalent to the pressure correction used in this work with the applied pressures agreeing well with our values (see Sec. II C 1 for details). The restoring force approach is similar to our correction of the local mode self-energy. Another difference is the auxiliary spring system for the correction of effects originating from the substituted unit cells, which is not included in the work of Mentzer *et al.* [14]. The reference simulation shows good agreement with our results as well as with the experimental data. For higher concentrations, our simulation yields slightly better comparison with the experimental data (i.e., lower transition temperatures), which can mainly be attributed to the marginally different pressure correction. However, a direct comparison should be made with caution since the distribution of Zr cations used in the reference simulation is not available.

2. Dielectric properties

Here, we use our MD simulations to calculate dielectric properties for the concentrations of 5% Zr (BZT05) and 50% Zr (BZT50). A simulation box size of $30 \times 30 \times 30$ was used for this purpose. The remaining settings for the MD simulations can be found in the previous section. Again, a cooling series was simulated for both systems, with the output configurations serving as input for the following temperature. The results for polarization as a function of temperature can be seen in Figs. 2(a) and 2(b). Ferroelectric behavior is observed for BZT05, with all three phase transitions of BT still clearly visible, albeit the spacing between transitions is closer than in pure BT case. The absolute values of the spontaneous polarization are in good agreement with experimentally observed values [34] and other simulations [14] from the literature. For the case of BZT50, no macroscopic polarization is detected, which means that the system remains in a nonpolar state for any simulated temperature. Furthermore, the strain tensor was examined, indicating that the system possesses cubic structure throughout all temperatures.

To calculate the susceptibility, we employed the scheme of Akbarzadeh *et al.* [13]. On the one hand, the susceptibility was determined by a direct method. For this purpose, an external field was applied during cooling MD runs in ⟨111⟩ direction with a maximum magnitude of 50 kV/cm. From this, the response of the system can be used to calculate the susceptibility in the respective directions. A reference simulation was performed for systems with spontaneous polarization to calculate the response induced purely by the applied external field. The corresponding formula reads

$$\chi_{\alpha\beta}^{\text{direct}} = \frac{NZ^*(\langle u_\alpha \rangle_{\text{ext}} - \langle u_\alpha \rangle_{\text{ref}})}{V\epsilon_0 E_{\text{ext},\beta}}. \tag{6}$$

Here, $\langle u_\alpha \rangle_{\text{ext}}$ is the average amplitude of the local mode when applying an external field E_{ext}. $\langle u_\alpha \rangle_{\text{ref}}$ represents the average amplitude of the reference simulation. α and β denote the Cartesian components of the local mode vector and the electric field vector. ϵ_0 is the vacuum permittivity. Z^* is the Born effective charge and V the volume of the supercell. N is the number of unit cells within the supercell. This susceptibility corresponds to the static limit. On the other hand, we use the dipole fluctuations as described by the correlation function (CF) to calculate the susceptibility:

$$\chi_{\alpha\beta}^{\text{CF}} = \frac{(NZ^*)^2}{V\epsilon_0 k_B T}(\langle u_\alpha u_\beta \rangle - \langle u_\alpha \rangle \langle u_\beta \rangle). \tag{7}$$

In this equation, u_i represents the Cartesian component of the local mode vector. T denotes the temperature and k_B is the Boltzmann constant. The obtained susceptibility can be

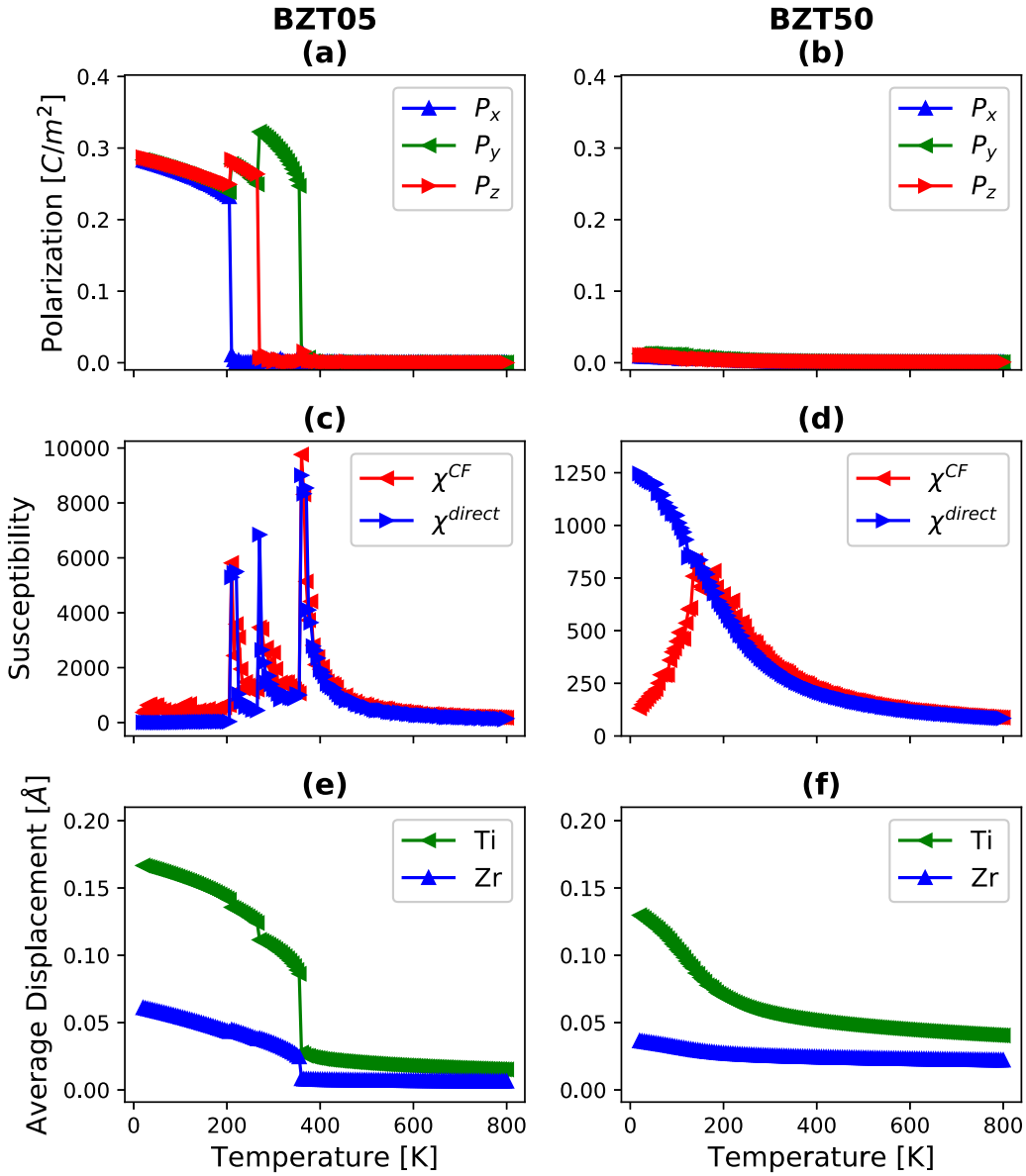

FIG. 2. Comparison of BZT05 (5% Zr) and BZT50 (50% Zr) in terms of the polarization (a),(b), the susceptibility (c),(d), and the average displacement of the two B-site species (e),(f). The susceptibility was calculated using a direct method and the correlation function (CF) describing fluctuations of the dipoles, respectively. The average displacement is calculated using the average absolute values.

referred to as the low-frequency dielectric response of the system [13].

The corresponding results are illustrated in Figs. 2(c) and 2(d). Here, we averaged the three diagonal components of the susceptibility tensor. In the case of BZT05, we observe good agreement between the two methods for determining susceptibility. The plot shows three peaks that can be assigned to the phase transitions of the parent system. It can already be seen that the individual transitions get closer to one other and lead to a possible diffuse transition between the paraelectric and ferroelectric phases. Furthermore, a Curie-Weiss (CW) behavior is found above T_c for both curves. For BZT50, a broad peak in χ^{CF} with a T_m of 180 K is observed, which is in good agreement with experimental data [35,36]. The static susceptibility shows a steady increase with decreasing temperature, with a tendency to flatten as low temperatures are approached. This behavior is consistent with experimentally measured patterns [37] in relaxor ferroelectrics. Furthermore, the results of BZT50 are in qualitatively good agreement with the simulations of Akbarzadeh *et al.* [13]. Nonetheless, we observe that the behavior of the static susceptibility in the low temperature region differs both in terms of shape, as well as in the absolute value as compared to Akbarzadeh *et al.* [13], if we apply moderate field strengths up to 50 kV/cm. Since the shape obtained in our work is more consistent with the experiment [37], we ascribe this difference to a more suitable choice of the applied external field strength. Hence, a comparison of the static susceptibility at the lowest temperature to Akbarzadeh is not necessary. Akbarzadeh *et al.* [13] provided an interesting analysis in the medium and high temperature regions. They reported that at temperatures above the Burns temperature T_b, both approaches (direct and CF) obey the

CW law, which we also observe (see more details in the Supplemental Material [27]). In our case, the fit of the CW law yields a T_0 of 140 K which is in reasonable agreement with an experimental value [35] of 114 K. They further reported that in the region below T_b down to $\sim$ 240 K the direct approach still follows the CW law, while CF starts to deviate. Finally, according to Ref. [13], both methods exhibit deviations from the CW law below 240 K. We can only partially confirm this peculiar behavior in the regions below T_b – in our case, a slight deviation between both methods is observed for this temperature range, but both methods start to deviate from the CW law for temperatures below $\sim$340 K. Unfortunately, it is not possible to trace down the origin of the discrepancy, however, we suspect it might be related to the parametrization of the model itself or the choice of the applied external field strength, which is consistent with the odd behavior of static susceptibility in the low temperature region.

To quantify the contribution to polarization by the different unit cells, the shifts of the B-site cations was calculated with respect to the center of mass of the oxygen octahedra. The basis for these calculations is MD simulations with the same settings described in detail in the previous section. The properties discussed further have been averaged over 600 ps. The relative displacement of the B-site cations can be seen in Figs. 2(e) and 2(f). In BZT05, it is clear that Ti atoms determine most of the polarization in BZT, while Zr atoms show only a slight off-centering. In our simulation of BZT25 (25% Zr content), at low temperatures, Ti ions are found to have an average displacement of 0.16 Å and Zr ions of 0.04 Å. That is in excellent agreement with values from a DFT study of $BaTi_{0.74}Zr_{0.26}O_3$ [38], which predicts a shift of 0.17 Å for Ti ions and 0.03 Å for Zr ions. In the case of BZT50, a slight off-centering of the B-site cations is observed throughout all simulated temperatures, increasing with decreasing temperature. In contrast to the work of Akbarzadeh *et al.* [13] we observe this increase not only for Ti but also for Zr ions. Although macroscopically there is no polarization of the system, the B-site ions shift to an energetically preferred position outside the center of the unit cell [28,38,39]. The increased off-centering at higher temperatures compared to BZT05 can be attributed to the expansion of the lattice, leading to increased activity of the local modes.

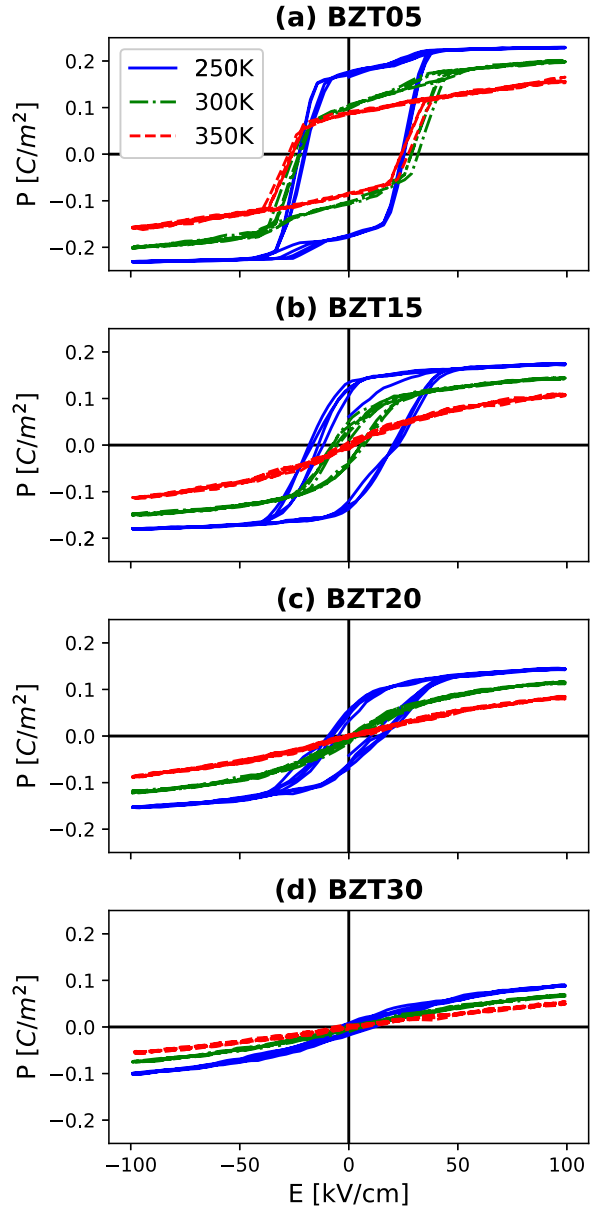

FIG. 3. Hysteresis loops of BZT05 (5% Zr), BZT15 (15% Zr), BZT20 (20% Zr) and BZT30 (30% Zr) at temperatures of 250, 300, and 350 K obtained from MD simulations.

3. Hysteresis loops

Here, we present simulated hysteresis loops of BZT05 (5% Zr), BZT15 (15% Zr), BZT20 (20% Zr), and BZT30 (30% Zr). For that purpose, a simulation box size of $30 \times 30 \times 30$ was chosen. The frequency of the oscillating field was set to 1 GHz, whereby the maximum field strength was 100 kV/cm, always applied along the $\langle 111 \rangle$ direction. For each composition and temperature several cycles were recorded. Figure 3 shows the hysteresis loops computed at the temperatures of 250, 300, and 350 K. In this figure, the net polarization is plotted. For BZT05, a classic ferroelectric behavior is observed at room temperature. Lowering the temperature leads to an increase in the saturated polarization and an increase in the remanent polarization. Increasing the temperature reduces the remanent polarization and the saturation polarization. In the case of BZT15, slightly above T_c a nonlinear trend of the hysteresis loop with zero remanent polarization is observed, which changes to a linear behavior when the temperature is increased further. We observe lower saturation polarization for a higher Zr content at the given temperature. Furthermore, hysteresis progressively dwindles and disappears entirely in the case of BZT30, leading to a linear dielectric behavior, as is expected by the increasing suppression of long-range ferroelectric order in BT by adding Zr. A comparison with experimental loops [40,41] from the literature shows that our simulated loops reproduce the general behavior of the BZT system, with absolute values of the saturation polarization in good agreement with the measured values. However, the associated field strengths are slightly overestimated in the simulated curves. This might be due to

the fact that the simulation assumes a perfect system where neither leakage currents nor other defects can occur.

Interestingly, the individual components of polarization (not shown) reveal that for concentrations between 10% and 20% of Zr, each of the three ferroelectric phases can be stabilized by applying external fields in certain directions. Indeed, it confirms that the three phases near the tricritical point are energetically very close to each other. This phenomenon has already been shown and discussed in detail by Mentzer *et al.* [14].

B. Simulations for BNT

1. Phase diagram

First, we use our parameterization for BNT to simulate the phase diagram. The settings of the MD simulations required for this are analogous to the phase diagram of BZT. Due to lack of experimental evidence on the distribution of Nb and V_{Ti} in BNT, we considered a spectrum of possible distributions and chose the one leading to the best match to experimental phase diagram. The choice of the final configuration was also motivated by previous DFT calculations of $5 \times 5 \times 5$ supercells performed applying complete structural relaxation, which indicated that (i) Nb cations tend to cluster randomly around Ti vacancies (four Nb atoms for one Ti vacancy) and that (ii) dissociated clusters (i.e., where Nb atoms are at least one nearest neighbor away from the Ti vacancy) are energetically slightly favorable [16]. For more details we refer readers to the Supplemental Material [27]. The results in Fig. 4(a) were obtained for a randomly distributed arrangement of Nb ions and Ti vacancies, which corresponds to the aforementioned dissociated clusters. Compared to BZT, a faster decrease in the transition temperature between the paraelectric and ferroelectric phases is observed here. Furthermore, the transition between the tetragonal and orthorhombic phases is flatter and almost constant up to the tricritical point. On the other hand, the transition between the orthorhombic and rhombohedral phases increases slightly. The tricritical point is found between 7.5% and 10% Nb content.

For comparison with experimental data, values from the literature as determined from dielectric measurements [42] are listed in Fig. 4(b). However, since these results do not show transition temperatures for all three phases, we also performed Raman measurements on BNT samples. These samples were prepared via the solid-state route and analyzed using a commercial Raman spectrometer. Details of both sample preparation and experimental parameters are reported elsewhere [43]. Raman spectra were collected as a function of temperature from $-196\,^{\circ}$C to $300\,^{\circ}$C using $25\,^{\circ}$C intervals. The phase diagram in Fig. 4(b) represents the resulting data. Compared to values from Ref. [42], a slightly higher transition temperature is observed for lower concentrations. However, a good agreement between the two experimental data is observed for higher concentrations. Comparison of the experimental data with the simulation data shows that the simulated transition temperatures agree very well for concentrations $<10\%$. For higher concentrations ($\geqslant 15\%$), the simulation slightly overestimates the experimental data. This can again be attributed to the applied pressure correction, which appears to be overestimated for higher concentrations.

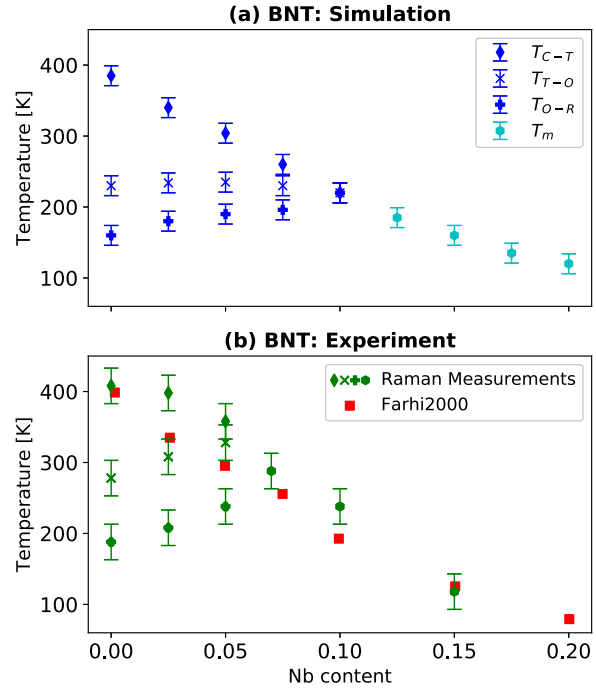

FIG. 4. Phase diagram of BNT as a function of concentration and temperature. (a) shows the simulated data. (b) experimental data obtained by Raman measurements (green symbols) and from dielectric measurements presented in literature [42] (red symbols). T_{C-T}, T_{T-O}, T_{O-R} transitions between cubic (C), tetragonal (T), orthorhombic (O), and rhombohedral (R) phases, respectively. T_m temperature of maximum in dielectric permittivity.

Overall, the simulation reproduces the phase diagram quite well.

2. Dielectric and structural properties

To further test the parametrization, dielectric properties and structural properties were calculated using MD on $30 \times 30 \times 30$ supercells for BNT05 and BNT15 (5% and 15% Nb content, respectively). Only lattice parameters for BNT15 were calculated using a larger ($96 \times 96 \times 96$) supercell size, as early tests showed that smaller supercell sizes (e.g. $30 \times 30 \times 30$) might lead to difficulties in the determination of lattice type in BNT15 due to the presence of local distortions. Large supercell sizes, in fact, statistically average local distortions and yield a cubic structure for temperatures between 20 and 800 K (for BNT15). That agrees well with experimental data [44] for Nb-substituted systems above a concentration of 12.5% Nb. For BNT05, a cubic phase is found at temperatures above 300 K. Furthermore, this system undergoes three phase transitions analogous to the parent system [see Fig. 5(a)]. The ground state at very low temperatures is a rhombohedral structure. The calculation of the static χ^{direct} as well as low-frequency susceptibility χ^{CF} is plotted in Figs. 5(c) and 5(d). For the calculation of the static susceptibility, an external field with a maximum amplitude of 50 kV/cm was applied in the $\langle 111 \rangle$ direction. Similar behavior can be seen for BNT05 as for BZT05. However, the transition temperatures are significantly lower than those of BZT05. For BNT15, χ^{direct} shows

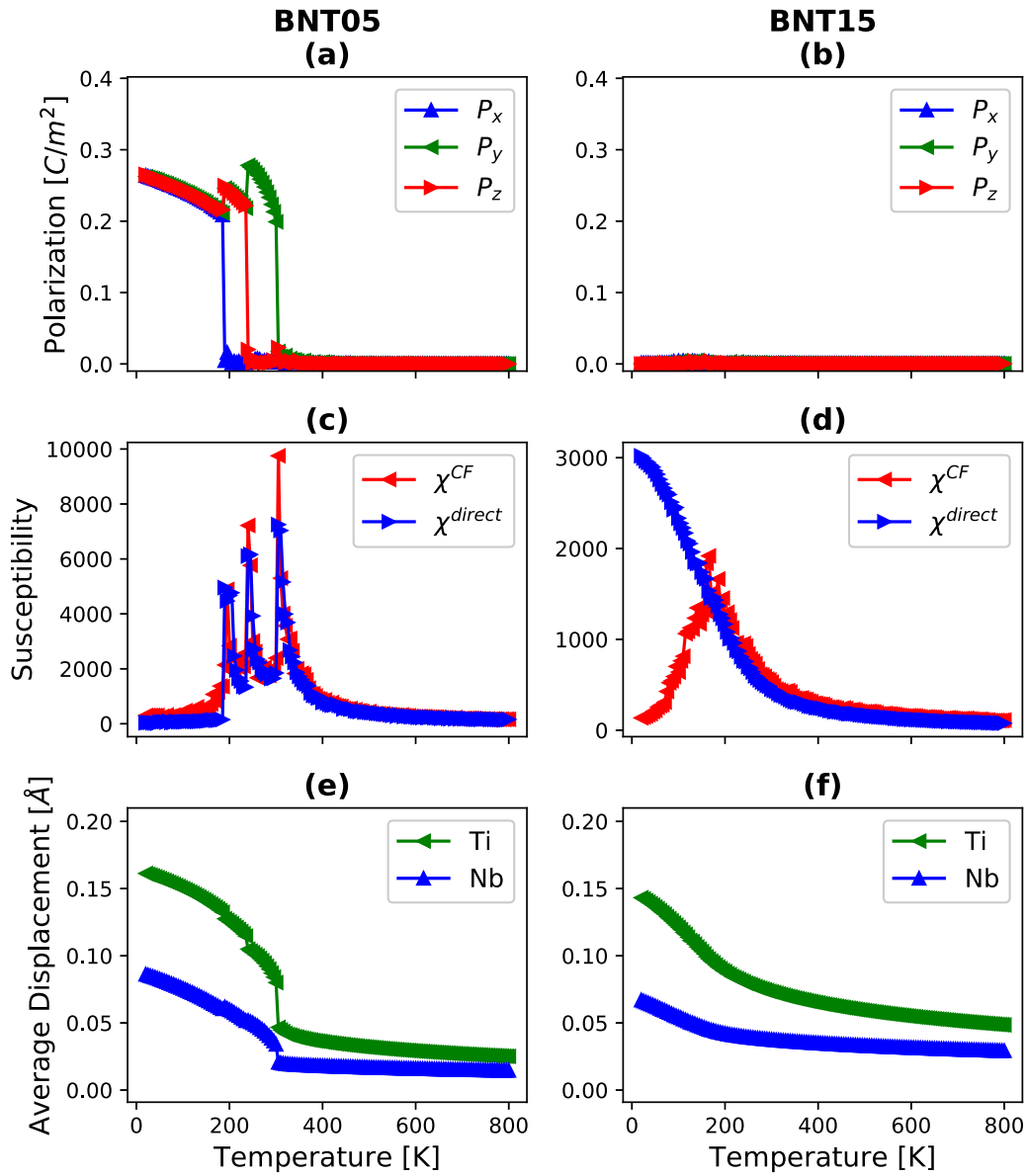

FIG. 5. Comparison of dielectric properties for BNT05 (5% Nb) and BNT15 (15% Nb). (a) and (b) show the polarization of the system. (c) and (d) show the susceptibility obtained from the direct method and the correlation function (CF) describing fluctuations of the dipoles, respectively. (e) and (f) show the average displacement of the individual B-site cations calculated using the average absolute values.

a typical relaxor behavior [37]. The corresponding χ^{CF} shows a broad peak with a T_m of 175 K. Such behavior was found earlier in BZT50 and suggests that in BNT the onset for relaxor behavior happens at less than 15% of Nb, as also confirmed experimentally [16,42]. Furthermore, a CW behavior for higher temperatures is observed for both systems above T_c and T_m, respectively.

Next, we focus on the averaged displacements of the B-site cations in BNT. The calculation of these displacements was carried out as described for BZT. Figures 5(e) and 5(f) show the shift for Ti and Nb ions in BNT05 and BNT15. Compared to BZT, Nb ions experience a significantly larger displacement than Zr ions. This local cation off-centering has already been confirmed by experiments [44]. It should be mentioned that a spontaneous polarization below 300 K is observed for BNT05 whereas BNT15 shows a nonpolar behavior [see Figs. 5(a) and 5(b), respectively). However, an averaged nonzero displacement is found in BNT15 at all temperatures simulated. That can be attributed to the lattice expansion through the applied pressure correction, similar to BZT50 and discussed in detail in Sec. III A 2. Furthermore, the fact that Nb shows a relatively large displacement also suggests that unit cells containing Nb at the B site may contribute substantially to the polarization. Hence, Nb unit cells may be considered only as a weak disruptor of the long-range ferroelectric correlation. In BNT, however, we need to consider also the presence of Ti vacancies, which indeed seem to affect the polar order in BNT significantly. Ti vacancies were considered as polar inactive in our parametrization, since DFT calculations found no significant contribution originating from the local mode,

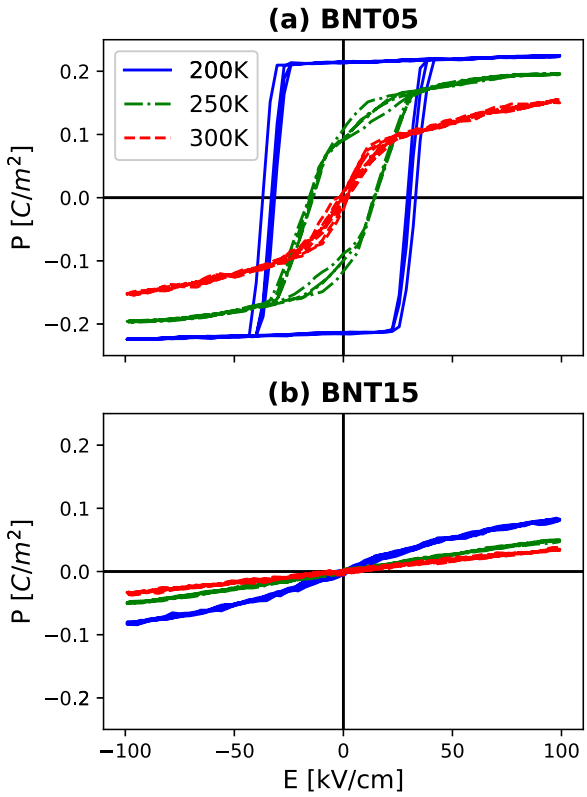

FIG. 6. Hysteresis loops of (a) BNT05 (5% Nb) and (b) BNT15 (15% Nb) at temperatures of 200, 250, and 300 K obtained from MD simulations.

i.e. nonpolar oxygen oscillation. However, these vacancies are considerably coupled to the surrounding unit cells, as described by the auxiliary spring system. That results in a constellation of V_{Ti} unit cells surrounded by unit cells with polarization biased in specific directions. These ensembles of unit cells can act as pinning centers for the surrounding ferroelectric matrix and thus can be considered as potential disruptors of the long-range ferroelectric order. In fact, increasing Nb concentration will increase the concentration of ferroelectrically inactive nanodomains centered on Ti vacancies, leading to overall disruption of the long-range correlation of B-site displacements.

In summary, the interplay between Ti vacancies and Nb unit cells as well as Ti unit cells appears to be responsible for the more effective disruption of long-range correlation within BNT compared to BZT.

3. Hysteresis loops

Finally, we consider hysteresis loops for BNT. Again, unit cells of size $30 \times 30 \times 30$ were used. The settings for the MD simulations are analogous to those of BZT. Figures 6(a) and 6(b) show the simulated hysteresis curves for BNT05 and BNT15 at different temperatures. For BNT05, a temperature of 200 K results in a saturated ferroelectric loop. When the temperature is increased, the remanent and the saturation polarization are reduced. A temperature close to the transition temperature (300 K) gives a nonlinear trend without showing a ferroelectric behavior anymore. Analogously to BZT, the application of an external field can also stabilize the ferroelectric phases of the parent system in the case of BNT. This indicates that also for the case of BNT the different phases close to the tricritical point are energetically very close to one other. For BNT15, a linear dielectric response is observed for temperatures above 250 K. At 200 K the loop shows a nonlinear behavior but without remanent polarization. Furthermore, in BNT15, no ferroelectric behavior can be induced by applying an external field.

IV. CONCLUSION

In this work, we carried out a parameterization of effective Hamiltonian models to describe the potential energy surface of BT-based substituted systems, which allowed the calculation of structural and electrical properties of the considered materials. The theoretical framework was based on the extension of our effective Hamiltonian approach for BT, considering substituting cations as perturbations of the parent system. First, we parametrized the homovalently substituted BZT system and presented a benchmark comparison with theoretical and experimental results from literature. Our model demonstrated good agreement with previous results on phase transitions, susceptibilities, and atomic displacement patterns. Only a slight overestimation of transition temperatures was found for high substituent contents, which was ascribed to the applied pressure correction and the Zr cation distribution. Following, the model was applied to the parametrization of the heterovalently substituted BNT system. The simulated phase diagram of BNT is in good agreement with our Raman measurements and experimental data from the literature. Furthermore, simulations have shown the onset of relaxor behavior at concentrations of about 15%, in good agreement to experiments. The associated structure remains macroscopically cubic and nonpolar for BNT15, and the dielectric behavior is in accord with experimental data for all simulated BNT compositions.

In summary, two parameter sets were presented which can be used for further studies on the investigated BZT and BNT systems, and can be adapted to represent other BT-based solid solutions. Since this approach requires only a small amount of computational effort, even very large supercells can be simulated in the future, leading to a realistic description and prediction of structural and electrical properties in BT solid solutions. The large-scale implementation of such simulations could become a decisive step towards the design of compositions with unprecedented properties.

ACKNOWLEDGMENTS

This project has received funding from the European Research Council (ERC) under the European Union's Horizon 2020 research and innovation program (Grant agreement No. 817190), and from the Austrian Science Fund (FWF): Project No. I4581-N. The computational results presented have been achieved in part using the Vienna Scientific Cluster (VSC). A. Ruban (KTH, Sweden) is acknowledged for supporting the calculation of effective cluster interactions in BZT and providing results of MC simulations. M.P. and J.S. gratefully acknowledge also the financial support under the scope

of the COMET program within the K2 Center "Integrated Computational Material, Process and Product Engineering (IC-MPPE)" (Project No. 859480). This program is supported by the Austrian Federal Ministries for Climate Action, Environment, Energy, Mobility, Innovation and Technology (BMK) and for Digital and Economic Affairs (BMDW), represented by the Austrian research funding association (FFG), and the federal states of Styria, Upper Austria and Tyrol. P.O. and J.H. acknowledge the Czech Science Foundation (Project No. 20–20326L).

[1] V. V. Shvartsman and D. C. Lupascu, J. Am. Ceram. Soc. **95**, 1 (2012).
[2] L. E. Cross, Ferroelectrics **151**, 305 (1994).
[3] V. Veerapandiyan, F. Benes, T. Gindel, and M. Deluca, Materials (Basel) **13**, 5742 (2020).
[4] R. D. King-Smith and D. Vanderbilt, Phys. Rev. B **49**, 5828 (1994).
[5] W. Zhong, D. Vanderbilt, and K. M. Rabe, Phys. Rev. B **52**, 6301 (1995).
[6] U. V. Waghmare and K. M. Rabe, Phys. Rev. B **55**, 6161 (1997).
[7] T. Nishimatsu, M. Iwamoto, Y. Kawazoe, and U. V. Waghmare, Phys. Rev. B **82**, 134106 (2010).
[8] A. Paul, J. Sun, J. P. Perdew, and U. V. Waghmare, Phys. Rev. B **95**, 054111 (2017).
[9] F. Mayer, M. N. Popov, D. M. Evans, S. Krohns, M. Deluca, and J. Spitaler, Phys. Rev. B **106**, 064108 (2022).
[10] L. Bellaiche, A. García, and D. Vanderbilt, Phys. Rev. Lett. **84**, 5427 (2000).
[11] L. Bellaiche and D. Vanderbilt, Phys. Rev. B **61**, 7877 (2000).
[12] L. Bellaiche, A. García, and D. Vanderbilt, Ferroelectrics **266**, 41 (2002).
[13] A. R. Akbarzadeh, S. Prosandeev, E. J. Walter, A. Al-Barakaty, and L. Bellaiche, Phys. Rev. Lett. **108**, 257601 (2012).
[14] C. Mentzer, S. Lisenkov, Z. G. Fthenakis, and I. Ponomareva, Phys. Rev. B **99**, 064111 (2019).
[15] T. Nishimatsu, A. Grünebohm, U. V. Waghmare, and M. Kubo, J. Phys. Soc. Jpn. **85**, 114714 (2016).
[16] V. Veerapandiyan, M. N. Popov, F. Mayer, J. Spitaler, S. Svirskas, V. Kalendra, J. Lins, G. Canu, M. T. Buscaglia, M. Pasciak, J. Banys, P. B. Groszewicz, V. Buscaglia, J. Hlinka, and M. Deluca, Adv. Electron. Mater. **8**, 2100812 (2022).
[17] T. Nishimatsu, U. V. Waghmare, Y. Kawazoe, and D. Vanderbilt, Phys. Rev. B **78**, 104104 (2008).
[18] K. M. Rabe and U. V. Waghmare, Phys. Rev. B **52**, 13236 (1995).
[19] J. H. Lee, U. V. Waghmare, and J. Yu, J. Appl. Phys. **103**, 124106 (2008).
[20] J. Paul, T. Nishimatsu, Y. Kawazoe, and U. V. Waghmare, Phys. Rev. Lett. **99**, 077601 (2007).
[21] P. E. Blöchl, Phys. Rev. B **50**, 17953 (1994).
[22] G. Kresse and J. Hafner, Phys. Rev. B **49**, 14251 (1994).
[23] G. Kresse and J. Furthmüller, Comput. Mater. Sci. **6**, 15 (1996).
[24] G. Kresse and J. Furthmüller, Phys. Rev. B **54**, 11169 (1996).
[25] G. Kresse and D. Joubert, Phys. Rev. B **59**, 1758 (1999).
[26] G. I. Csonka, J. P. Perdew, A. Ruzsinszky, P. H. T. Philipsen, S. Lebègue, J. Paier, O. A. Vydrov, and J. G. Ángyán, Phys. Rev. B **79**, 155107 (2009).
[27] See Supplemental Material at http://link.aps.org/supplemental/10.1103/PhysRevB.106.224109 for tables of parameters, additional MD simulations, and analysis of susceptibilities.
[28] I. Levin, E. Cockayne, V. Krayzman, J. C. Woicik, S. Lee, and C. A. Randall, Phys. Rev. B **83**, 094122 (2011).
[29] J. Kreisel, P. Bouvier, M. Maglione, B. Dkhil, and A. Simon, Phys. Rev. B **69**, 092104 (2004).
[30] A. A. Bokov, M. Maglione, and Z.-G. Ye, J. Phys.: Condens. Matter **19**, 092001 (2007).
[31] C. Laulhé, F. Hippert, J. Kreisel, M. Maglione, A. Simon, J. L. Hazemann, and V. Nassif, Phys. Rev. B **74**, 014106 (2006).
[32] Andrei Ruban (private communication, 27 January 2022).
[33] L. Dong, D. S. Stone, and R. S. Lakes, J. Appl. Phys. **111**, 084107 (2012).
[34] H. H. Wieder, Phys. Rev. **99**, 1161 (1955).
[35] T. Maiti, R. Guo, and A. S. Bhalla, J. Am. Ceram. Soc. **91**, 1769 (2008).
[36] J. Petzelt, V. Bovtun, D. Nuzhnyy, M. Kempa, M. Savinov, M. Paściak, S. Kamba, G. Canu, and V. Buscaglia, Phys. Status Solidi B **258**, 2100259 (2021).
[37] A. Levstik, Z. Kutnjak, C. Filipič, and R. Pirc, Phys. Rev. B **57**, 11204 (1998).
[38] C. Laulhé, A. Pasturel, F. Hippert, and J. Kreisel, Phys. Rev. B **82**, 132102 (2010).
[39] A. Bootchanont, J. Jutimoosik, S. Chandarak, M. Unruan, S. Rujirawat, R. Yimnirun, R. Guo, and A. Bhalla, Ceram. Int. **39**, 579 (2013).
[40] Z. Yu, R. Guo, and A. S. Bhalla, J. Appl. Phys. **88**, 410 (2000).
[41] Q. Xu and Z. Li, Process. Appl. Ceram. **14**, 188 (2020).
[42] R. Farhi, M. El Marssi, A. Simon, and J. Ravez, Eur. Phys. J. B **18**, 605 (2000).
[43] V. K. Veerapandiyan, S. Khosravi H, G. Canu, A. Feteira, V. Buscaglia, K. Reichmann, and M. Deluca, J. Eur. Ceram. Soc. **40**, 4684 (2020).
[44] K. Page, T. Kolodiazhnyi, T. Proffen, A. K. Cheetham, and R. Seshadri, Phys. Rev. Lett. **101**, 205502 (2008).